Geothermics 124 (2024) 103145

Contents lists available at ScienceDirect

Geothermics

journal homepage: www.elsevier.com/locate/geothermics

# Modeling the impact of natural roughness of tension joints on heat transport

Benoit Nigon [a,*], Christophe Pascal [b], Andreas Englert [b,†]

[a] Univ Rouen Normandie, UNICAEN, CNRS, M2C UMR 6143, F-76000 Rouen, France
[b] Institute of Geology, Mineralogy and Geophysics, Ruhr University Bochum, Germany

ARTICLE INFO

*Keywords:*
Natural fracture
Numerical modeling
Fluid flow
Heat exchange
Taylor dispersion

ABSTRACT

The understanding of heat transport in fractures is crucial for mining geothermal systems. Studies of heat transport in natural fractures at scales comprised between those of laboratory experiments and those of field tracer tests are seldom. To bridge the gap, a joint surface with characteristic plumose was scanned in the field using LiDAR technology. The scanned surface was used to build a numerical model of mode 1 fracture. Fluid flow and heat transport were modeled solving the steady-state Stokes equation and assuming Fourier transport, respectively. We considered three different fracture apertures and varied systematically roughness in order to investigate the impact of plumose on fluid and heat transport. The 3D velocity flow fields were characterized by mean hydraulic aperture and by statistics on the directional components of the velocity vector. The method of temporal moments was used to extract first and second moments from temperature breakthrough curves. Heat transport parameters (local and macroscopic) were calculated from first and second moments.

We show that hydraulic aperture and the longitudinal component of the velocity vector decrease with increasing roughness. The local variation of heat transport parameters is controlled by fracture roughness. For the macroscopic transport parameters, several transport regimes were identified. At low fracture aperture (i.e. 1 mm), conductive regime dominates heat transport in agreement with low Péclet numbers. In this case, fracture roughness affects the transport parameters via the loss of hydraulic aperture. With higher aperture (i.e. 3 mm) geometrical dispersion regime is dominant, roughness controlling the amplitude of transport parameters. At 5 mm aperture, transition from geometrical to Taylor dispersion occurs and the roughness tends to decrease dispersion and dispersivity according to the mean flow velocity.

## 1. Introduction

Gaining better understanding on flow and transport processes in fractures plays an important role for improving feasibility and sustainability of $H_2$, $CO_2$ and nuclear waste storage (e.g. *Neretnieks, 1980*; *Wang and Narasimhan, 1985*), and exploitation of natural resources (e.g. *Gautam and Mohanty, 2004*). The characterization and prediction of heat plume behavior in fractured networks is decisive for the development of e.g. Enhanced Geothermal Systems (EGS), exploiting the heat circulating in both liquid and solid phases of a reservoir. Indeed, the understanding of heat transfer between fluid and rock matrix remains a major challenge for efficient heat exploitation (*Heinze et al., 2017*; *Frank* et al., *2021*).

Heat transport in porous or fractured media was shown to be analogous to solute transport (*Bons* et al., *2013*; *Gossler* et al., *2019*). As such, there are similarities between Fickian and Fourier transports (*Geiger and Emmanuel, 2010*). Anomalous solute transport caused by heterogeneities within the porous/fractured medium (i.e. non-Fickian transport, *Bromly and Hinz, 2004*; *Berkowitz* et al., *2006*; *Gouze* et al., *2008*; *Fomin* et al., *2011*) find their counterparts in the propagation of heat plumes (i.e. non-Fourier transport, *Geiger and Emmanuel, 2010*). The key difference between solute and heat transport takes its origin in the diffusion of heat. The latter is several orders of magnitude faster than solute diffusion in water (*Geiger and Emmanuel, 2010*; *Cherubini* et al., *2017*). Furthermore, heat is considered to propagate at a velocity approximatively equal to Darcy's velocity (*Geiger and Emmanuel, 2010*).

* Corresponding author.
*E-mail address:* nigonben@univ-rouen.fr (B. Nigon).
† Now at Department of Applied Geology, Institute of Geosciences and Geography, Martin Luther University Halle-Wittenberg, Von-Seckendorff-Platz 3, 06120 Halle, Germany.

https://doi.org/10.1016/j.geothermics.2024.103145
Received 21 December 2023; Received in revised form 10 July 2024; Accepted 16 August 2024
Available online 29 August 2024

Conflicting descriptions of thermal dispersivity exist (*Anderson, 2005; Ma* et al., *2012; Rau* et al., *2012; Cherubini* et al., *2017*). For some authors, heat transport is dominated by thermal conductivity for low flow rates (*Woodbury and Smith, 1985*; *Cherubini* et al., *2017*). *Vandenbohede* et al. *(2009)* and *Constantz* et al. *(2003)* found that thermal dispersivity was significantly smaller than solute dispersivity. In contrast *De Marsily (2004) and Molina-Giraldo (2001)* found thermal dispersivity to be of the same order as solute dispersivity. *De Marsily (2004)* suggested significant departure between both dispersivities at large scales, for which thermal dispersion was expected to reach an asymptotic value. *Bons* et al. *(2013)* compared and linked thermal and solute transport. They defined dispersion regimes in function of the Péclet number in laminar flow: (1) the molecular diffusion regime (Pe < 0.1–0.3), (2) the transition regime (0.1–0.3 < Pe < 5), (3) the major regime (5 < Pe < 250–4000) and (4) the pure mechanical dispersion regime (250–4000 < Pe).

The effects of the parabolic velocity profile on dispersion (i.e. the Taylor-Aris dispersion) add another level of complexity in fractures (Taylor, 1953; *Bouquain* et al., *2011*). Shortly after solute/heat injection, the parabolic velocity profiles induce longitudinal spreading of plumes. Such a spreading is considered to enhance transverse mixing and to counteract advective spreading (*Bouquain* et al., *2011*). Later after injection, diffusion leads to homogenization of the plume along fracture width. For solute transport in single fractures, *Roux et al. (1998)* and *Detwiler* et al. *(2000)* identified several modes of dispersion in fractures as a function of the Péclet number. For increasing Péclet numbers, dominant dispersion modes exhibit a transition from molecular dispersion (i.e. Pe < 1, conduction for heat) via macro-dispersion (i.e. intermediate regime) to Taylor dispersion for large Péclet numbers.

In spite of a wealth of research works addressing real fracture network geometries (e.g. *Pascal* et al., *1997*; *Bonnet* et al., *2001*) and heat transport in fractured networks (*Geiger and Emmanuel, 2010; Luo* et al., *2016; Cherubini* et al., *2017, 2018*), heat and solute transport studies have been traditionally conducted on single open fractures at laboratory scales (*Auradou* et al., 2010; *Fourar and Radilla*, 2009; *Zou* et al., 2017; *Luo* et al., 2018; *Luo* et al., *2019*), whose upscaling to typical reservoir/outcrop scales is not straightforward. At macroscopic scales, flow and heat transport were modeled based on the extrapolation of fracture geometries assuming self-affine properties (*Neuville* et al., *2010*, *2011*; *Liu* et al., *2020*) or investigated in the field using tracer tests (*Read* et al., *2013*; *Klepikova* et al., *2016*; *Guihéneuf* et al., *2017*). Most recent investigations of the influence of fracture roughness on heat transport have considered statistically simulated fractures surfaces *(Klepikova* et al. *2021; Jaoude* et al. *2022; Okoroafor* et al. *2022)* or fracture surfaces resulting from mechanical testing of rock samples *(Chen and Zhao 2020; Chen* et al. *2022)*, however and to our best knowledge, modeling heat transport at the scale of a single fracture including realistic geometries gathered in the field has never been attempted.

In this study, we investigate thermal transport in a natural tension joint. The geometry of one of the fracture walls was numerically restored based on LiDAR scans *(Nigon* et al. *2017)*. We built a 3D fracture model by means of creating the missing wall as mirror image of the originally scanned one *(Nigon* et al. *2019)*. Series of models involving three apertures, three roughness amplitudes and similar pressure gradients were computed. Fracture flow was calculated using the Stokes equation for stationary regimes and characterized using hydraulic aperture and the variance of the directional components of the velocity vector. Heat transport was calculated assuming Fourier transport and considering convection and conduction. Velocity fields resulting from fracture flow modeling were used for the convective term of heat transport models. In the following, we first introduce the methods and tools of the study before detailing and discussing the modelling results.

## 2. Methods

Fracture flow was computed using the Stokes equation (*Mourzenko* et al., *1995*; *Adler* et al., *2013*):

$$-\nabla P + \mu \nabla^2 u = 0 \tag{1}$$

where P is pressure, $\mu$ viscosity and u fluid velocity. The Stokes equation is a simplification of the Navier-Stokes equation for which the inertial term is neglected.

The presence of plumose on the joint surface proves that it is a mode 1 fracture (i.e. opening strictly perpendicular to fracture walls, e.g. *Pascal 2021*). Thus, in order to construct an open fracture model, we assumed that the missing wall surface was the mirror image of the measured one. We considered the mechanical aperture being the mean distance separating both surfaces.

In order to estimate hydraulic aperture at model scale, we used mean flow velocity from the model as in *Nigon* et al. *(2019)*:

$$\alpha_h = \sqrt{\frac{24 U_{avg} \eta L}{2P}} \tag{2}$$

where $\alpha_h$ is hydraulic aperture, L fracture length according to the main direction of flow, P pressure difference between inlet and outlet of the model, η viscosity, and $U_{avg}$ equivalent average velocity in the fracture.

To model heat transport in the fracture we computed convection and conduction based on Fourier transport, as in *Geiger and Emmanuel (2010)* and *Rau* et al. *(2012)*:

$$\frac{\partial T}{\partial t} = \nabla [vT + D_a \nabla T] \tag{3}$$

where $D_a$, v, t, and T indicate thermal dispersion, fluid velocity in the fracture, time, and temperature, respectively.

The temporal moment method was adopted to analyze heat transport breakthrough curves (i.e. BTCs). For each cross-section in the fracture, approximately 10.000 heat transport BTCs were extracted. Normal and log-normal distributions were tested as in *Cirpka and Kitanidis (2000a)* and *González-Pinzón* et al. *(2013)*. After calculating the root-mean-square-error for each BTC, we found that BTCs were best fitted by log-normal distribution.

Using the mean μ and the standard deviation σ of the log-normal distribution, mean time and variance of BTC are classically estimated from the first and the second moment respectively:

$$m_1 = \mathrm{e}^{\mu + \left(\frac{\sigma^2}{2}\right)} \tag{4}$$

$$m_2 = e^{\left(\sigma^2 - 1\right)} \mathrm{e}^{\left(2\mu + \sigma^2\right)} \tag{5}$$

In the quasi one-dimensional case the apparent velocity $v_a$, the apparent dispersion coefficient of mixing $D_a$, and the apparent dispersivity of mixing $\alpha_a$ for each individual BTC are (*Cirpka and Kitanidi 2000a*):

$$\mathrm{v_a} = \frac{\mathrm{L} m_0}{\mathrm{M}}, \tag{6}$$

$$\mathrm{D_a} = \frac{\mathrm{V} * \mathrm{v_a^3}}{2 m_0 \mathrm{L}}, \text{ and} \tag{7}$$

$$\alpha_{\mathrm{a}} = \frac{\mathrm{D_a}}{\mathrm{v_a}} \tag{8}$$

L being distance to injection source and $m_0$ the zero-order moment.

The previous parameters correspond to path-averaged values related to mixing in the fracture domain. According to *Cirpka and Kitanidis (2000b)*, $m_0$ remains constant within the entire domain for the quasi one-dimensional case.

However, in case of tracer tests or laboratory studies, BTCs are traditionally measured at outflow. Hence, the results represent an integration of the apparent transport parameters. To determine the flux-

weighted average and spreading of temperature at model scale, weighted moments were calculated:

$$m^{*}_{1mac} = M \quad (9)$$

$$m^{*}_{2mac} = V + \sigma^2 \quad (10)$$

The two moments allowed for calculating the macro-dispersion parameters, that is, macroscopic seepage velocity, macro dispersion coefficient and macro dispersivity coefficient, respectively:

$$v_{mac} = \frac{Lm_0}{M^{*}_{1mac}}, \quad (11)$$

$$Da_{mac} = \frac{L^2 M^{*}_{2mac} * m_0^2}{2M^{*}_{1mac^3}} \quad (12)$$

$$Disp_a = \frac{D_{amac}}{v_{mac}} \quad (13)$$

The Péclet number in fractures is calculated as a function of the aperture, flow velocity and molecular diffusion (*Detwiler* et al., *2003*). For heat transport, molecular diffusion is replaced by thermal diffusivity (*De Marsily, 2004*; *Bons* et al., *2013*), thus, the Péclet number can be re-written:

$$Pe = \frac{v_{frac} a_h}{\alpha} \quad (14)$$

where $v_{frac}$ represents average velocity according to X (i.e. longitudinally), α thermal diffusivity and $a_h$ hydraulic aperture.

A methodology based on the work of *Roux* et al. *(1998)* and *Detwiler* et al. *(2000)* was adopted in order to describe dispersion regimes in our models. This methodology takes into account thermal diffusivity and variation in heat plume velocity along the plane and across the width of the fracture (Taylor dispersion):

$$D_{L,Taylor} = \frac{v^2_{frac} a^2_h}{210\alpha} \quad (15)$$

*Roux* et al. *(1998)* used scaling arguments to identify three primary dispersion regimes: the molecular diffusion regime, the geometric dispersion regime and the Taylor dispersion regime. Following *Roux* et al. *(1998) and Detwiler* et al. *(2000)*, this scaling relationship may be written:

$$\frac{Da_{mac}}{\alpha} = \tau + Disp_a Pe + Disp_{Taylor} Pe^2 \quad (16)$$

where $\tau$ is the tortuosity for diffusion in the fracture and $Disp_{Taylor}$ Taylor dispersion.

## 3. Model configuration and convergence study

We scanned the surface of a joint using terrestrial LiDAR technology (*Nigon* et al., *2017*). The selected fracture surface had been freshly exhumed in the Klieve quarry, Münsterland, western Germany. The joint surface morphology was identified as a S-type plumose structure, characterized by quasi-symmetrical structures and a straight propagation axis. Joint surface elevation (with respect to its mean plane) varied between −2.7 and 3.7 mm with a standard deviation of 1.2 mm. Further details may be found in (*Nigon* et al., *2017*). To study the impact of the fine features of the joint surface, we focused on a sample 600mm×600 mm. The dimensions are admittedly below those of typical field tests, however, the aim of our modelling was to investigate flow and heat transport at fracture scale as a step to future upscaling.

The 3D fracture geometry was constructed considering the missing joint surface as the mirror image of the originally scanned one. Three mechanical apertures, i.e. 1, 3 and 5 mm, were selected, the latter apertures reflecting realistic values at typical geothermal reservoir depths (e.g. *Agheshlui* et al., *2018*). Our modeling addressed: (1) a "parallel plate configuration" (i.e. fracture with smooth walls), as reference, (2) a natural roughness configuration, as described above, and (3) an amplified natural roughness configuration. The amplified natural roughness configuration was constructed by multiplying by two the amplitudes of the relief of the natural roughness configuration. Modeled geometries reproduced natural ones with unprecedented fidelity.

Fracture flow and heat transport were computed with a Finite Element Method (FEM) implemented in the commercial software Comsol Multiphysics v5.2, which involved an iterative solver (i.e. Multigrid Method) for flow and a direct solver (i.e. MUMPS, Anon., *Comsol, 2012*) for heat transport. Fracture surfaces were meshed with triangular elements and the volume between fracture walls with tetrahedral ones. The combination of three mechanical apertures with three fracture surfaces resulted in nine models. Each heat transport model required approximately 40 h of computation on a PC with 16 GB of RAM and a 3.2 GHz Intel i5 processor.

Fracture flow and heat transport were calculated in two steps. Firstly, fracture flow was computed using Stokes equation for stationary regimes and, secondly, the resulting velocity field was used in the modeling of heat transport. In more detail, pressures of 1 Pa and 0 Pa were set at fracture inlet and outlet respectively, resulting in a gradient of 1.6 Pa·$m^{-1}$ for all modeled configurations (Fig. 1).

Fluid viscosity and density were set to $10^{-3}$ Pa·s and 1000 kg·$m^{-3}$ respectively. Initial fracture temperature was 293.15 K (i.e. 20 °C), whereas the temperature of the injected fluid was equal to 363.15 K (i.e. 90 °C). Both convection and conduction were modeled, adopting thermal diffusivity and conductivity values of 1.54 $10^{-7}$ $m^2$ $s^{-1}$ and 0.63 W $m^{-1}$ $K^{-1}$, respectively, for the injected water. To note, because the lateral edges of the modeled fracture had been set to slip boundary conditions, fracture surfaces equilibrated instantaneously to water temperature (i.e. reached thermal equilibrium).

In order to validate our models, a mesh convergence study was performed for all calculated configurations of rough fracture walls (Fig. 2a). When the number of elements was increased, the mean flow velocity of the configurations "5 mm, 1X natural roughness" and "5 mm, 2X natural roughness" converged to $3.15{\cdot}10^{-3}$ m $s^{-1}$ and $2.9{\cdot}10^{-3}$ m $s^{-1}$ respectively. The latter tests suggested that the solutions were satisfactory for at least $3.9{\cdot}10^{6}$ elements for both configurations (Figs. 2b, 2c and 2d). For the heat transport models, the increase in number of elements was investigated as a function of the BTCs for a cross-section perpendicular to the main flow direction (see red line in Fig. 2a). The heat transport models converged (Figs. 2e and 2f) where the local transport parameters were calculated using the extreme BTC values (see also Appendix 1, Figs. A1 and A2).

Comparing the minimum (maximum) local heat transport velocity value of the model involving $1.08{\cdot}10^{6}$ elements with its counterpart of the model involving $4.2{\cdot}10^{6}$ elements (see also Appendix 1, Figs. A1 and A2), we found that the percentage of variation between both values was 0.94 % (1.33 %). However, when comparing minimum (maximum) local dispersion and minimum (maximum) local dispersivity, the percentage of variation was respectively 20.53 % (19.26 %) and 21.43 % (20.14 %). The latter results suggested that, although the transport models converged, the numerical errors led to errors in dispersion for the extreme values of 20.53 % for local dispersion and 21.43 % for local dispersivities (i.e. the configuration "5 mm, 2X natural roughness" was the most computationally demanding model).

In addition to the previous 3D models that integrated fracture geometries with rough surfaces, series of 2D heat transport models were computed. Indeed, the 3D fracture models using plane fracture walls were equivalent to and could be simplified to a 2D section along the X-Z plane. Thus, computation time was drastically reduced and a higher number of "parallel plate configuration" models for several apertures could be calculated. The results of these simplified models contributed to elucidate the general behavior of parameters such as thermal dispersivity as function of hydraulic aperture in the 3D models.

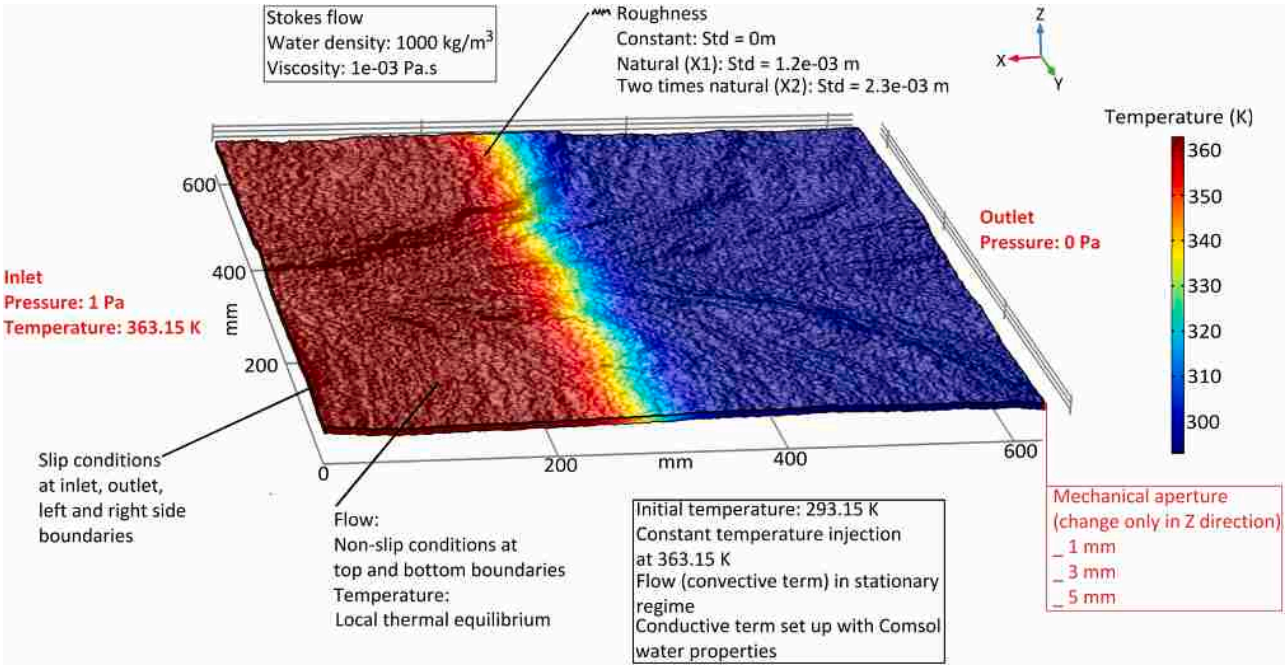


**Fig. 1.** Setup of the numerical model.

## 4. Flow characterization

We characterized the modeled fracture flow fields in function of hydraulic aperture and statistical analyses of 3D flow velocity vector (Fig. 3). The very first and expected result was that introduction of fracture surface roughness led to systematic hydraulic aperture decrease (Fig. 3a), and the more pronounced the roughness the more the mechanical and the hydraulic apertures diverged. For example, in the case of the 5 mm mechanical aperture, hydraulic aperture was 5 mm for the "parallel plate configuration" (as anticipated) but only ~4.7 mm for the "2X natural roughness configuration".

In addition, we compared theoretical and modeled velocity variances, focusing on the X component (Fig. 3a). Our results pointed to a clear correspondence between both, evidencing that velocity variance is strongly submitted to hydraulic aperture, even for the extreme "2X natural roughness configurations". The standard deviations of velocities along Y and Z (Figs. 3b and 3c) computed with the parallel plate configuration were converging to 0 $m{\cdot}s^{-1}$, in prefect agreement with theoretical considerations. However, for rough fracture surface models (i.e. "1X and 2X natural roughness"), standard deviations increased both with aperture and surface roughness.

## 5. Heat transport analysis

### 5.1. Heat transport in a single fracture

The characterization focused on the local transport parameters and showed how they developed as a function of distance from injection. Fig. 4 depicts the results of the heat transport modeling carried out for the configuration "5 mm, 2X natural roughness". The heat transport was studied along six cross-sections perpendicular to the main flow direction (i.e. X) at distances from the fracture inlet of 100 mm to 600 mm in steps of 100 mm. Typically, the BTC analysis for a single cross-section consisted in extracting a total amount of 11,000 to 12,000 BTCs. Each single BTC was fitted with a theoretical log-normal distribution that served to extract the temporal moments. For example, Fig. 4a shows the result of the fitting procedure when applied to each individual BTC for the 500 mm cross section. Fit quality was estimated with RMS errors for all configurations presented in the paper. Boxplots in Fig. 4b summarize the RMS errors estimated for the configuration "5 mm, 2X natural roughness". Based on the median values of the RMS error distributions (i.e. comprised between $0.45{\cdot}10^{-3}$ and $2.25{\cdot}10^{-3}$, Fig. 4b), the modeled BTCs showed acceptable fit with their theoretical counterparts. The worst fit quality was found close to the heat injection boundary (i.e. at 100 mm), it remained nevertheless within a tolerable range.

For all modeled configurations the RMS errors showed similar trends as for the "5 mm, 2X natural roughness" case. Local results showed mean transport time increasing linearly with distance (Figs. 4c and 4e). Relatively short mean heat transport times were typically modeled along the joint propagation axis (i.e. at a cross-sectional Y distance of ~300 mm, Fig. 2a). The longer local mean heat transport times were found at ~ 200 and ~400 mm cross-sectional Y distance. These locations were associated with the highest horizontal curvature in fracture wall relief and changes in roughness (Fig. 2a). The results at 200 and 400 mm cross-sectional Y distance showed marked symmetry, reflecting the effects of the quasi-elliptical geometry of the plumose.

The results of our models clearly showed the variability of mean transport arrival times across fracture width. Due to the parabolic velocity profile in the fracture, the mean transport times were relatively short by its center, where velocity peaked, and relatively long close to its edges. These local impacts were also observed for other local transport parameters and configurations. Local perturbations of the variance of the heat transport BTC (Fig. 4d and 4f) resulting from roughness showed variations similar to the local heat transport mean times.

The local dispersion (Fig. 4g and 4i) and the local dispersivity (Figs. 4h and 4j) showed comparable local perturbations in function of roughness. However, variability in local dispersion as well as in local dispersivity was also linked to fracture aperture. The width of the band (here, the term band is used to describe values normal to the mean flow direction in Figs. 4c, 4d, 4g and 4h) was related to both velocity parabolic profile and fracture roughness. Consequently, local heat transport mean time, local variance, local dispersion and local dispersivity varied also as a function of vertical position (i.e. Z coordinate) in the fracture.

Local dispersion and local dispersivity means increased slightly with distance from injection. The variances of local dispersion and local dispersivity decreased with increasing distance to fracture inlet (Figs. 4g and 4h), as it was also documented by the decrease of the 25 % and 75 % quantiles' difference from the median (Fig. 4i and 4j). However, local

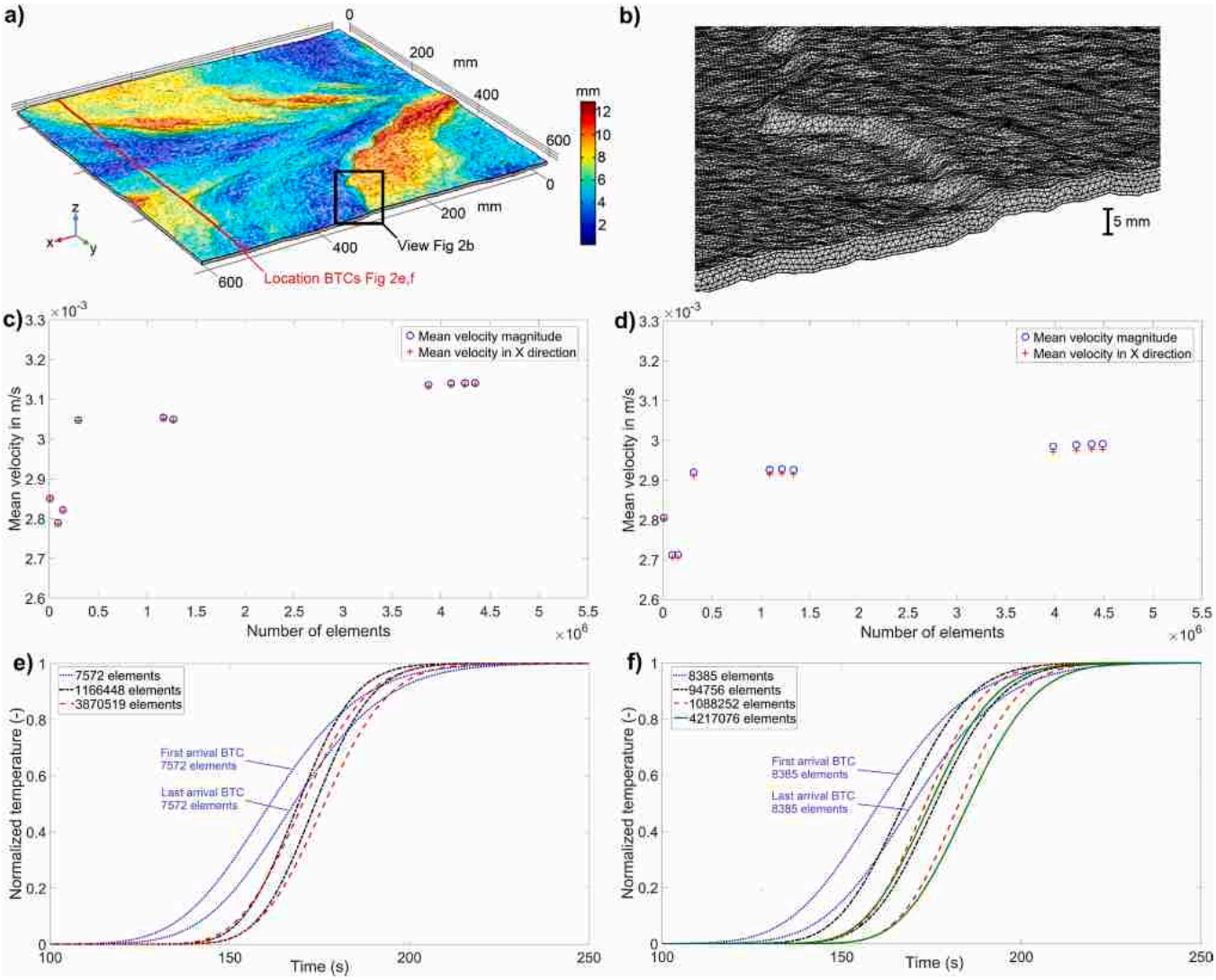


**Fig. 2.** Validation of the models. a) 3D view of the joint with locations of b), e) and f). b) Mesh used in flow and heat transport analysis for the configuration "5 mm aperture, 2X natural roughness". c) Mesh convergence analysis considering flow velocity magnitude and flow velocity along X for the configuration "5 mm, 1X natural roughness". d) Same as in c) for the configuration "5 mm, 2X natural roughness". e) Mesh convergence analysis on heat transport for the configuration "5 mm, 1X natural roughness". f) Same as in e) for the configuration "5 mm, 2X natural roughness".

dispersion and local dispersivity stabilized after ~ 400 mm cross-section.

### 5.2. Impact of roughness on heat transport

The shortest mean arrival time as well as the largest spreads for the BTC curves were modeled for the parallel plate configuration (i.e. constant aperture case in Fig. 5). When natural roughness was introduced in the models, heat transport times and BTC variances were respectively longer and lower with respect to the parallel plate configuration. Noteworthy, when natural roughness was amplified by a factor of two, mean transport time further increased and BTC variance decreased.

In the following we will discuss quantitatively the 5 mm aperture cases in comparison to the 3 mm and 1 mm aperture cases. According to the cubic law the local heat transport mean time is controlled by the inverse of the cube of the fracture aperture, as Fig. 6a suggests. In agreement with previous fracture flow characterizations (*Renshaw, 1995*; *Mourzenko* et al., *1995*; *Ge, 1997*; *Chen* et al., *2017*), our results showed that the use of rough fracture surfaces affected mean flow velocity and hydraulic aperture. Consequently, for a given mechanical aperture heat transport mean times were shorter for the parallel plate configuration than for the rough fracture wall ones. Furthermore, heat transport mean times were shorter for the 1X natural roughness configuration than for the 2X natural roughness configuration (e.g. Fig. 5).

In our models, two trends can be observed (Fig. 6b). For the 1 mm and 3 mm mechanical aperture configurations, the local BTC variance for the parallel plate configuration was smaller than the local variance of the 1X and 2X natural roughness configurations. For the 5 mm configuration this trend was reversed, i.e. the local variance of the parallel plate configuration was higher than these of the 1X and 2X natural roughness configurations. We will further discuss the effect below.

Considering macroscopic properties, mean transport velocities were controlled by the cube of fracture aperture for the parallel plate configuration and decreased when rough fracture walls were modeled (Fig. 7a). Concerning the local values (i.e. error bars in Fig. 7a) a higher standard deviation of transport velocity was simulated close to the fracture inlet. Expectedly, standard deviation decreased with distance from injection.

The local dispersion and macro-dispersion values were generally constant along the main flow direction for each modeled case (Fig. 7b). However, for the 5 mm configurations, dispersion increased slightly

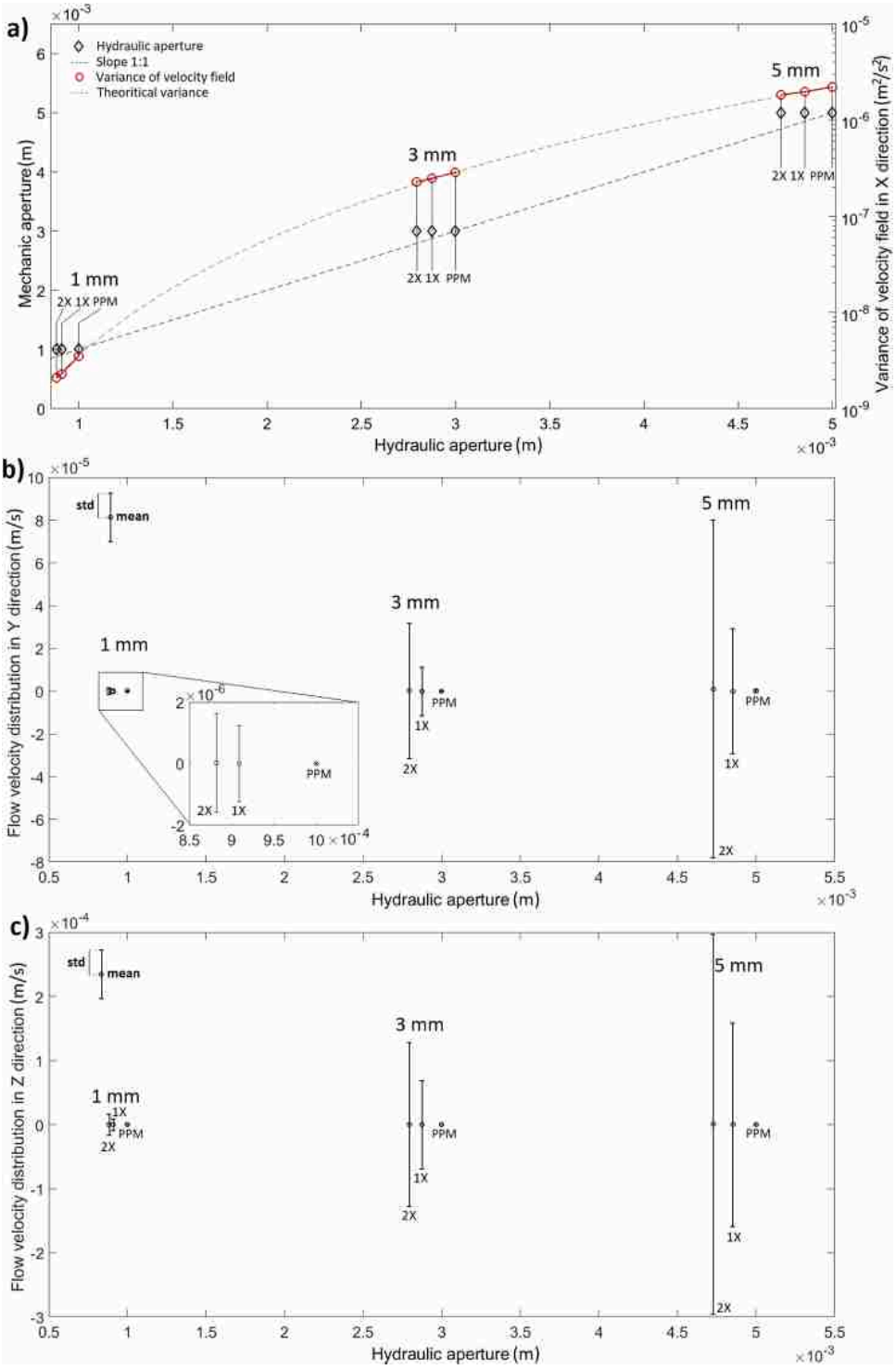


**Fig. 3.** Fracture flow analysis based on three mechanical apertures (i.e. 1, 3 and 5 mm), a parallel plate configuration (i.e. PPM) and two rough fractures (i.e. "1X and 2X natural roughness configurations", see text for details). a) Composite diagram depicting the relationships between mechanical aperture and modeled hydraulic aperture and between variance of velocity field (X component), its theoretical variance and modeled hydraulic aperture. b) Mean and standard deviation of the velocity field (Y component). c) Same as in b) for the Z component.

until ~400 mm distance from fracture inlet. Local and macro dispersion increased with fracture aperture. Interestingly, two trends emerged from the modeling of rough fractures (Fig. 7b). For the 1 mm configuration, the local and macro dispersion increased with roughness amplitude, however, for the 5 mm configuration they decreased with roughness amplitude. The 3 mm configuration delivered a mix of both trends: adding a rough surface increased the macro dispersion and the local dispersion (Fig. 7b). Increasing mechanical aperture produced decrease in local dispersion. However, the macro-dispersion of the 3 mm configuration increased with increasing roughness.

The variations of dispersivity with aperture were more difficult to interpret (Fig. 7c). As anticipated, macro dispersivity was predicted to be higher than the mean value of the local dispersivities. Focusing on individual mechanical aperture configurations, dispersivity trends

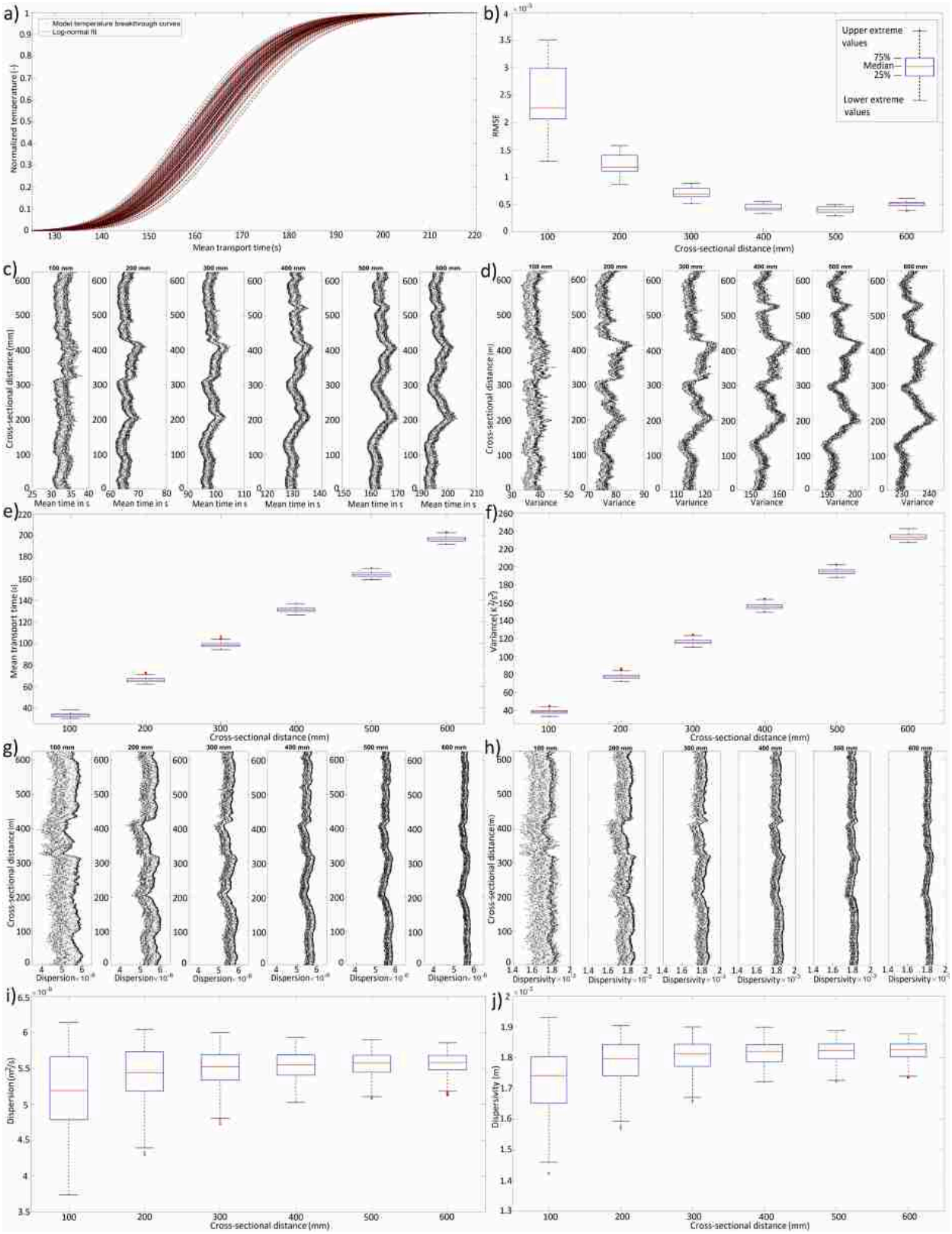


**Fig. 4.** Example of heat transport analysis for the configuration "5 mm, 2X natural roughness", for the sake of clarity only 100 BTCs are shown and six cross-sections perpendicular to main flow are considered (see Fig. 2a for locations and model geometry). a) Example of BTCs fitted with log-normal cumulative distributions (results at 500 mm longitudinal X distance). b) Box plot of root-mean-square error (BTC vs log-normal fit). c) Heat transport mean times, d) BTC variance calculated from moment analysis. e) Statistical plot of heat transport mean time. f) Statistical plot of BTC variance. g) Local dispersion. h) Local dispersivity. i) Statistical plot of dispersion. j) Statistical plot of dispersivity. All quantities presented in c) to j) were calculated from moment analysis.

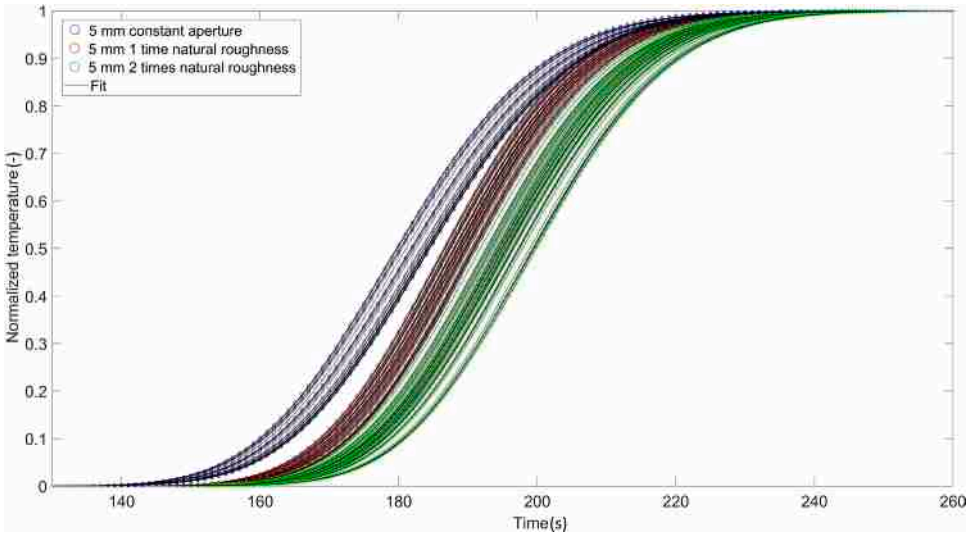


**Fig. 5.** Examples of temperature breakthrough curves (BTCs) as a function of time at 600 mm from fracture inlet and for 5 mm aperture.

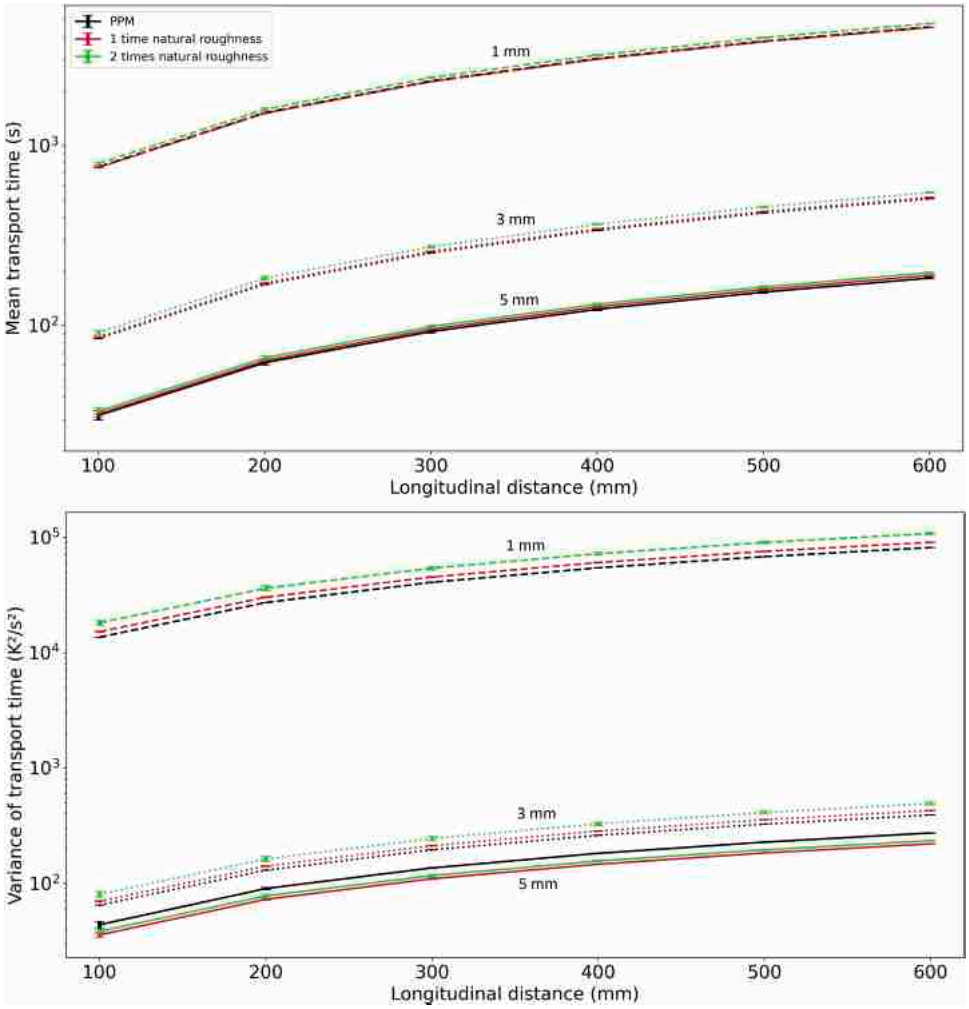


**Fig. 6.** a) local mean heat transport time and b) local variance in function of longitudinal distance. All results are presented for the 1 mm, 3 mm and 5 mm configurations and considering roughness variations.

resulting from introduction of roughness in the models were similar to the ones found for dispersion. For 1 mm mechanical aperture, dispersivity increased with roughness (Fig. 7c). A similar behavior was obtained in models involving 3 mm mechanical aperture. For 5 mm aperture, dispersivity decreased with roughness. However, values of macro dispersion for the configuration "5 mm, 2X natural roughness"

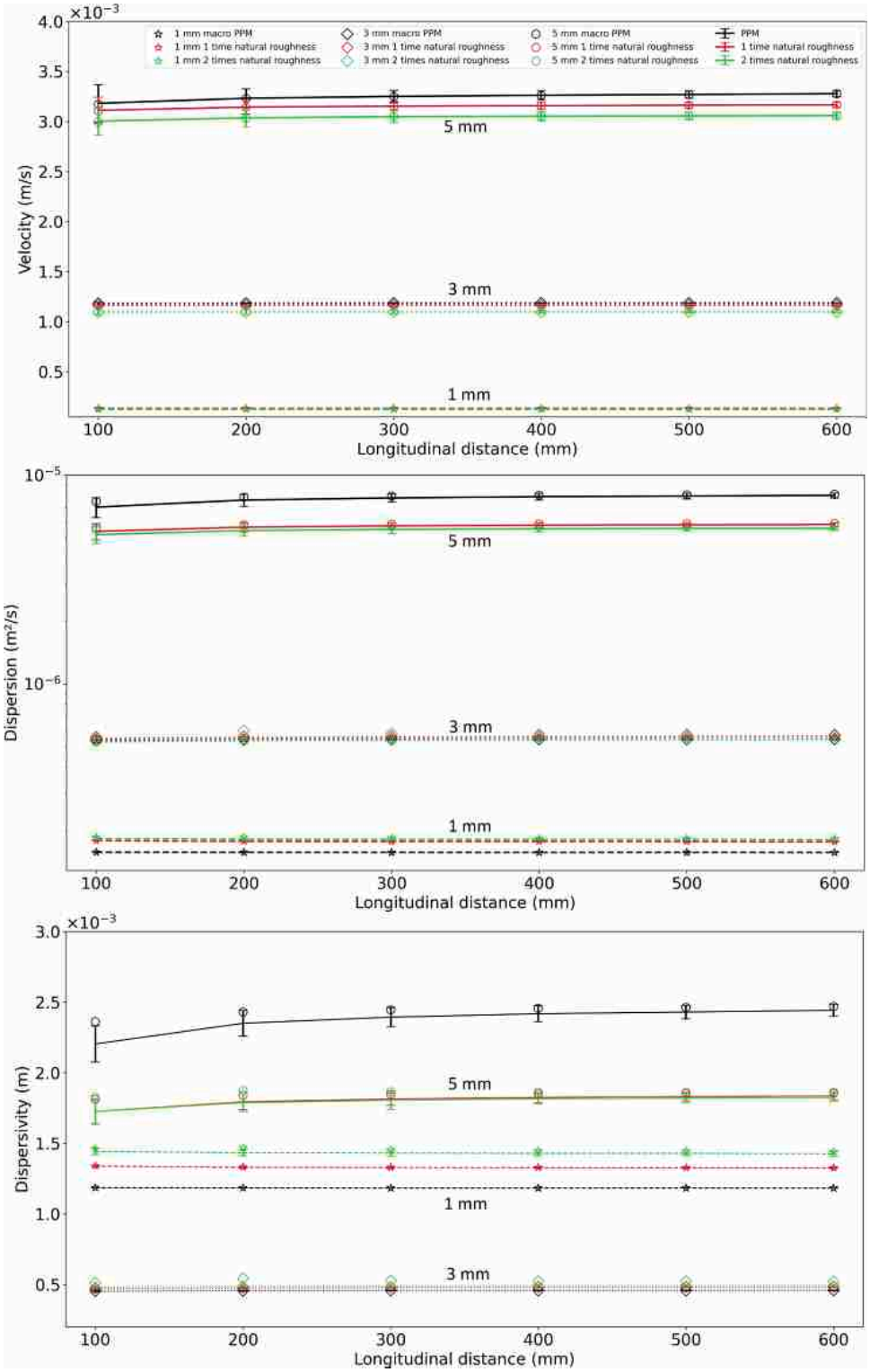


**Fig. 7.** a) velocity, b) dispersion and c) dispersivity for the 1 mm, 3 mm and 5 mm mechanical aperture configurations and variable roughness.

were slightly higher than the ones for "5 mm, 1X natural roughness". As a general rule, dispersivity dropped when mechanical aperture varied from 1 mm to 3 mm, independently of the other parameters. When the aperture was further increased to 5 mm, an increase in dispersivity occurred.

### 5.3. Comparison with previous studies

In the following we compare our heat transport results with previous theoretical and experimental studies. We first summarize our results on dispersivity and dispersion together and supplement them with additional numerical modeling results of heat transport for the 2D parallel plate configuration (Fig. 8).

For similar pressure gradients, dispersivity decreased when

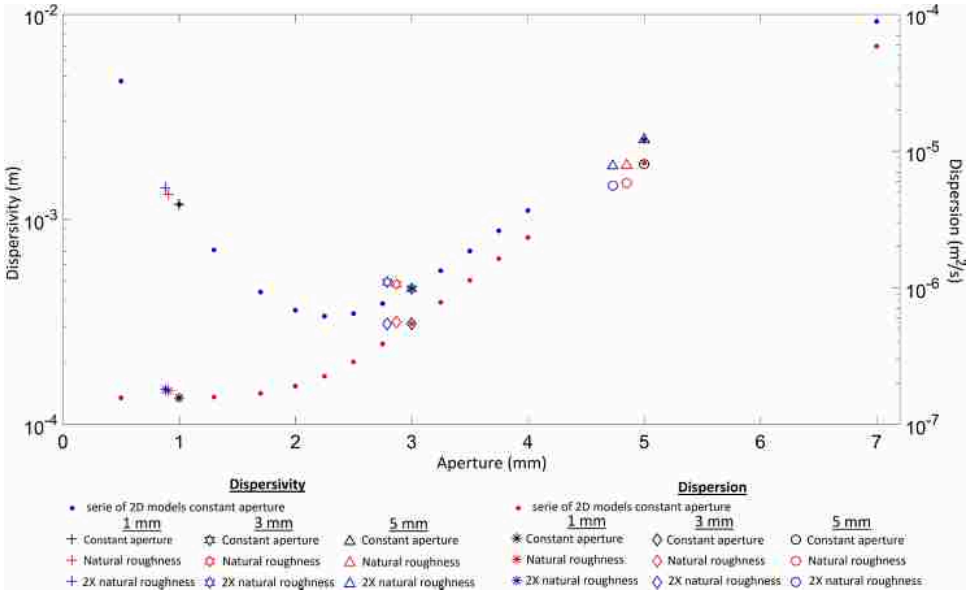


**Fig. 8.** Macro dispersion and macro dispersivity for series of parallel plate models and different mechanical apertures compared to the results of models with rough fracture surfaces.

increasing mechanical aperture from 0.5 to ~2.1 mm (Fig. 8a). After reaching its minimum at about 2.1–2.3 mm aperture, dispersivity increased again. Dispersion was constant between 0.5 mm and 1.75 mm but increased for larger apertures (Fig. 8b). In brief, Fig. 8 evidences several dispersion regimes as already advanced by *Roux* et al. *(1998)* and *Detwiler* et al. *(2000)*, yet for solute transport in fractures.

To allow for detailed comparison, we plotted our results as proposed by *Detwiler* et al. *(2000)* and by *Roux* et al. *(1998)* in Fig. 9a and 9b, respectively. In Fig. 9a, macrodispersion was scaled by the mean flow velocity multiplied by the mechanical aperture of the fracture. In Fig. 9b, macrodispersion was scaled according to thermal diffusivity. *Roux* et al. *(1998)* and *Detwiler* et al. *(2000)* constructed their respective plots by varying Péclet number with increasing flow velocity/pressure. However, in our study, we varied fracture aperture and surface roughness. In Fig. 9a, the variation of $D_{amac}.\nu^{-1}.\ a_h^{-1}$ in function of Péclet number follows a straight line with a slope of −1 for the 1 mm configuration, suggesting that heat transport is chiefly controlled by conduction in the case of low apertures. At the other end, our modeling suggested that heat transport behavior approached the Taylor dispersion regime for the 5 mm configuration. We note, however, that our computed values are slightly below the ones advanced by *Detwiler* et al. *(2000)*.

For the 5 mm configurations, our models predict values of $D_{amac}.\nu^{-1}.\ a_h^{-1}$ (i.e. the weighted dispersion, Fig. 9) lower than those obtained considering solute dispersion and the simplified parallel plate configuration (*Detwiler* et al. *2000*). When 1X natural roughness was modeled, the value of $D_{amac}.\nu^{-1}.\ a_h^{-1}$ decreased with respect to the constant aperture model. However, in case of the 2X natural roughness configuration, $D_{amac}.\nu^{-1}.\ a_h^{-1}$ increased compared to the 1X natural roughness models. Concerning the 3 mm models, our results plotted in the macro dispersion regime (Fig. 9a), according to the scheme of *Detwiler* et al. *(2000)*. Noteworthy, $D_{amac}.\nu^{-1}.\ a_h^{-1}$ was found to increase with roughness in the latter case.

Interestingly, all our parallel plate model results agree very well with the function proposed by *Roux* et al. *(1998)* (Fig. 9b, Eq. (16)). The ratios $Da_{mac}/\alpha$ (i.e. macrodispersion scaled by thermal diffusivity) for the 1 mm configurations were found close to 1 indicating conduction regime. However, the ratios $Da_{mac}/\alpha$ for the 3 mm configurations were higher than the ones found for the 1 mm configurations, furthermore they increased with aperture. In more detail, $Da_{mac}/\alpha$ increased with roughness for 1 mm aperture but did not show significant variation for 3 mm aperture. For 5 mm aperture, $Da_{mac}/\alpha$ decreased with roughness, however all values approached reasonably well the proposed fit.

## 6. Discussion

### 6.1. Physical meaning of the results

Our results of fracture flow characterization show deviation from the cubic law when adding roughness to the models in line with numerous previous studies (e.g. *Mourzenko* et al., *1995*; *Renshaw, 1995*; *Ge, 1997*; *Chen* et al., *2017*). Hydraulic aperture and mean velocity in the longitudinal direction decrease with roughness. This decrease becomes more significant when roughness is further increased (i.e. for the 2X natural roughness configuration).

*Gelhar* et al. *(1992)* compiled the dispersivities obtained in various studies of porous and fractured media. Their work was later completed by *Zhou* et al. *(2007)*, who furthermore showed that dispersivity was scale-dependent. Our dispersivity estimations, between $4.5{\cdot}10^{-4}$ m and $2.5{\cdot}10^{-3}$ m for a fracture length of 625.5 mm, are perfectly in-line with the values reported by *Gelhar* et al. *(1992)* and *Zhou* et al. *(2007)*. They are, however, slightly below their counterparts for solute transport. Nevertheless, in contrast to the predictions of *Constantz* et al. *(2003)* and *Vandenbohede* et al. *(2009)*, our modeled thermal dispersivities do not deviate significantly from values commonly accepted for solute ones. Indeed, they fall in the same order of magnitudes as those advanced by *De Marsily (2004)*. Thus, our results support the assumption of *De Marsily (2004)*, who proposed that both solute and thermal dispersivities exhibited similar orders of magnitude. Noteworthy, our estimations of the ratio $D_{amac}.\nu^{-1}.\ a_h^{-1}$ (Fig. 9a) underestimate moderately the values for the theoretical Taylor dispersion regime proposed by *Detwiler* et al. *(2000)*.

For the 1 mm configuration, the ratio $D_{amac}.\nu^{-1}.\ a_h^{-1}$ can clearly be related to a conduction-dominated regime (Fig. 9a). Rough fractures act on thermal dispersion through the decrease in hydraulic aperture as a function of roughness (amplitude), and differences in transport parameter values between parallel plate and rough fracture configurations are controlled by changes in hydraulic aperture. However, variations of flow velocities at the location of the hackles do not significantly impact the behavior of the heat plume.

For the 3 mm aperture configuration, our results correspond to the power-law/macro dispersion regime as it was defined by *Roux* et al.

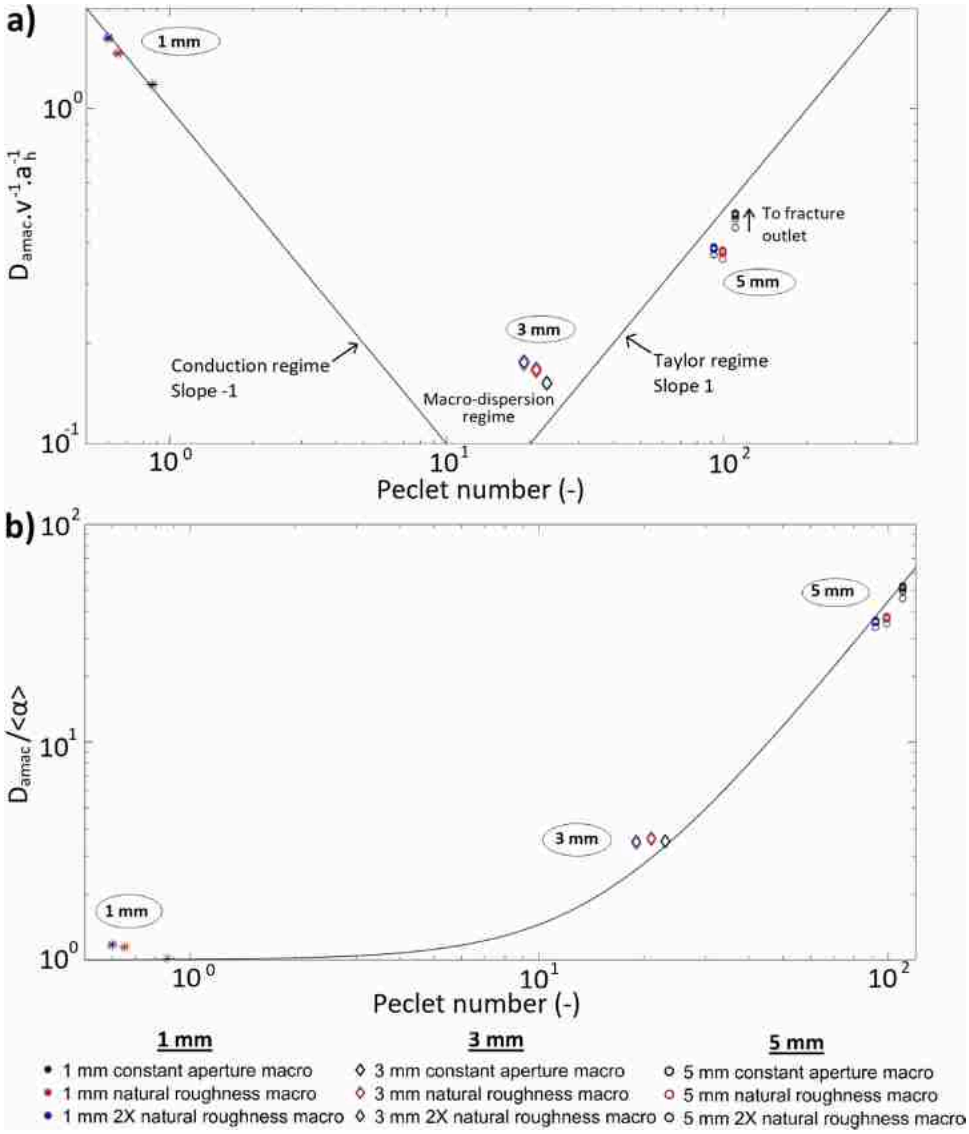


**Fig. 9.** Transport results compared to theory for cross sections perpendicular to the main flow direction. a) Macrodispersion weighted according to mechanical aperture multiplied by mean flow velocity in function of Péclet number as proposed by *Detwiler* et al. *(2000)*. b) Macrodispersion scaled by thermal diffusivity in function of Péclet number as proposed by *Roux* et al. *(1998)*. The results are plotted for all the six cross-sections considered in this study. For the 1 and 3 mm aperture cases all six cross-sections yield similar results, for a given roughness configuration. However, for the 5 mm case the results tend to converge to the Taylor dispersion regime (as proposed in Detwiller et al. 2000) for cross-sections approaching to outlet. The fit displayed in Fig. 9b was created using a thermal dispersivity of $2.5{\cdot}10^{-3}$ m (equal to the estimated dispersivity for the 5 mm parallel plate configuration), $\tau = 1$ (corresponding to the ordinate at the origin) and a Taylor dispersivity of $4.3{\cdot}10^{-3}$ m (corresponding to the best fit for the constant aperture configurations).

*(1998)* and *Bons* et al. *(2013)*. Increasing roughness increases the ratio $D_{amac}.v^{-1}.a_h^{-1}$ but does not affect significantly the ratio $D_{amac}/\alpha$ (Fig. 9). However, increasing roughness promotes deviation from the ideal fits depicted in Fig. 9. Increasing roughness increases also thermal dispersivity (Fig. 7c) but the impact of roughness on thermal dispersion is less significant. Such a behavior may be interpreted in terms of the anomalous regime described by *Roux* et al. *(1998)*. Here, heat transport is subject to geometrical dispersion and roughness controls the amplitude of transport parameters together with hydraulic properties. In addition, hackles add a local and supplementary heterogeneity compared to a variable aperture field for a mode 1 fracture.

For the 5 mm configuration, models with rough walls show thermal dispersion values and thermal dispersivities slightly lower than those of the parallel plate model. The increase in $D_{amac}.v^{-1}.a_h^{-1}$ and $D_{amac}/\alpha$ with distance from fracture inlet (suggested by the vertical arrow in Fig. 9a) seems to be related to the transition from pre-asymptotic dispersion regime to Taylor dispersion (*Taylor, 1953*). However, this behavior is also influenced by the distance to the injection boundary. In general, from the 3 mm configuration to the 5 mm one we observe a transition from geometrical to Taylor dispersion regime (following the classification of Detwiler et al. 2000). In this case we observe that the use of rough surfaces decreases dispersion and dispersivities for a similar pressure gradient at the inlet of the fracture.

### 6.2. *Accuracy of the computations*

It is common practice in numerical studies to benchmark the results against analytical solutions. Analytical solutions are, by nature, only available for simplified configurations of the studied system. In the present case, we validated successfully the modeling results of the idealized parallel plate configurations against their analytical counterparts (see e.g. Fig. 8 and Nigon et al. 2019). However, to our best knowledge there is no analytical solution available for flow and heat transport through rough fractures. In order to circumvent the problem,

we conducted a thorough mesh convergence study (see §3 and Appendix 1). The procedure was not ideal in itself but suggested anyhow that the numerical errors were at least two orders of magnitude smaller than velocity statistical estimates (see also discussion in Nigon et al. 2019). Furthermore, the consistency and the physical soundness of our results comforts us on their validity. In particular, the remarkable agreement between our findings and the first-order predictions of Roux et al. (1998) and Detwiler et al. (2000), as shown in Fig. 9, can hardly be fortuitous.

## 7. Conclusion

Our study aimed at characterizing heat transport in a mode 1 fracture with S-type plumose. Fracture flow was modeled based on Stokes equation. Convective and conductive heat transport were calculated according to the Fourier transport equation. Heat transport parameters were determined from estimation of the temporal moments. Local transport parameters were computed for mean transport time, variance of BTC, apparent dispersion and apparent dispersivity.

Our first-order results agree with those obtained in previous studies on the impact of surface roughness and hydraulic aperture on heat transport in fractures. However, the present work, involving a real (scanned) joint surface, allowed for investigating the impact of natural features of the fracture surface on heat transport. The latter was out of reach in previous studies that considered synthetic self-affine or log-normal aperture fields, in general.

The present results show that (1) hydraulic aperture and the longitudinal component of the velocity vector decrease with increasing roughness, (2) the local variation of heat transport parameters is controlled by fracture roughness, and (3) several transport regimes exist for the macroscopic transport parameters. In detail, conductive regime dominates heat transport at low fracture aperture (i.e. 1 mm) but with increasing aperture (i.e. 3 mm) geometrical dispersion regime is dominant, roughness controlling the amplitude of transport parameters. At 5 mm aperture, transition from geometrical to Taylor dispersion occurs and the roughness tends to decrease dispersion and dispersivity according to the mean flow velocity.

## CRediT authorship contribution statement

**Benoit Nigon:** Writing – review & editing, Writing – original draft, Visualization, Validation, Investigation, Formal analysis, Conceptualization. **Christophe Pascal:** Conceptualization, Methodology, Writing – review & editing. **Andreas Englert:** Writing – review & editing, Writing – original draft, Supervision, Project administration, Funding acquisition, Formal analysis, Conceptualization.

## Declaration of competing interest

The authors declare that they have no known competing financial interests or personal relationships that could have appeared to influence the work reported in this paper.

## Data availability

Data will be made available on request.

## Acknowledgements

The authors are thankful to Thomas Heinze (Ruhr University Bochum) for his comments on a previous version of the manuscript. The first author benefited from a PhD grant from the Applied research on enhanced Geothermal Energy System (AGES) graduate school, a joint venture between the International Geothermal Centre Bochum (GZB) and the Institute of Geology, Mineralogy and Geophysics, Ruhr University Bochum. We thank Mandy Duda and Rolf Bracke (GZB) for their support.

## Appendix 1

| Configuration | Velocity (m/s) | Dispersion ($m^2/s$) | Dispersivity (m) |
|---|---|---|---|
| First 7572 | $3.38 \cdot 10^{-3}$ | $1.47 \cdot 10^{-5}$ | $4.33 \cdot 10^{-3}$ |
| Last 7572 | $3.25 \cdot 10^{-3}$ | $1.30 \cdot 10^{-5}$ | $4.00 \cdot 10^{-3}$ |
| First 1.1 M | $3.24 \cdot 10^{-3}$ | $4.80 \cdot 10^{-6}$ | $1.48 \cdot 10^{-3}$ |
| Last 1.1 M | $3.15 \cdot 10^{-3}$ | $4.46 \cdot 10^{-6}$ | $1.41 \cdot 10^{-3}$ |
| First 3.8 M | $3.21 \cdot 10^{-3}$ | $6.02 \cdot 10^{-6}$ | $1.87 \cdot 10^{-3}$ |
| Last 3.8 M | $3.11 \cdot 10^{-3}$ | $5.49 \cdot 10^{-6}$ | $1.76 \cdot 10^{-3}$ |

**Fig. A1.** Local transport parameters from the mesh convergence analysis on heat transport for configuration: 5 mm and 1X natural roughness (Fig. 2e).

| Configuration | Velocity (m/s) | Dispersion ($m^2/s$) | Dispersivity (m) |
|---|---|---|---|
| First 8385 | $3.34 \cdot 10^{-3}$ | $1.46 \cdot 10^{-5}$ | $4.30 \cdot 10^{-3}$ |
| Last 8385 | $3.21 \cdot 10^{-3}$ | $1.26 \cdot 10^{-5}$ | $3.90 \cdot 10^{-3}$ |
| First 94756 | $3.27 \cdot 10^{-3}$ | $6.98 \cdot 10^{-6}$ | $2.13 \cdot 10^{-3}$ |
| Last 94756 | $3.11 \cdot 10^{-3}$ | $5.85 \cdot 10^{-6}$ | $1.88 \cdot 10^{-3}$ |
| First 1.08 M | $3.16 \cdot 10^{-3}$ | $4.87 \cdot 10^{-6}$ | $1.54 \cdot 10^{-3}$ |
| Last 1.08 M | $3.00 \cdot 10^{-3}$ | $4.31 \cdot 10^{-6}$ | $1.44 \cdot 10^{-3}$ |
| First 4.2 M | $3.13 \cdot 10^{-3}$ | $5.87 \cdot 10^{-6}$ | $1.87 \cdot 10^{-3}$ |
| Last 4.2 M | $2.96 \cdot 10^{-3}$ | $5.14 \cdot 10^{-6}$ | $1.73 \cdot 10^{-3}$ |

**Fig. A2.** Local transport parameters from the mesh convergence analysis on heat transport for configuration: 5 mm and 2X natural roughness (Fig. 2f).

## References


Adler, P.M., Thovert, J.F., Mourzenko, V.V., 2013. Fractured Porous Media. Oxford University Press. ISBN 978-0-19-966651-5.

Anderson, M.P., 2005. Heat as a ground water tracer. Ground Water 43 (6), 951–968. https://doi.org/10.1111/j.1745-6584.2005.00052.x.

Agheshlui, H., Sedaghat, M.H., Matthai, S., 2018. Stress influence on fracture aperture and permeability of fragmented rocks. J. Geophys. Res. Solid Earth 123, 3578–3592. https://doi.org/10.1029/2017JB015365.

Auradou, H., Boschan, A., Chertcoff, R., D'Angelo, M.-V., Hulin, J.-P., Ippolito, I., 2010. Miscible transfer of solute in different model fractures: from random to multiscale wall roughness. C.R. Geosci.. 342 (7–8), 644–652. https://doi.org/10.1016/j.crte.2009.03.003.

Berkowitz, B., Cortis, A., Dentz, M., Scher, H., 2006. Modeling non-Fickian transport in geological formations as a continuous time random walk. Rev. Geophys. 44 (2), 3293. https://doi.org/10.1029/2005RG000178.

Bonnet, E., Bour, O., Odling, N.E., Davy, P., Main, I., Cowie, P., Berkowitz, B., 2001. Scaling of fracture systems in geological media. Rev. Geophys. 39 (3), 347–383. https://doi.org/10.1029/1999RG000074.

Bons, P.D., van Milligen, B.P., Blum, P., 2013. A general unified expression for solute and heat dispersion in homogeneous porous media. Water Resour. Res. 49 (10), 6166–6178. https://doi.org/10.1002/wrcr.20488.

Bouquain, J., Meheust, Y., Davy, P., 2011. Horizontal pre-asymptotic solute transport in a plane fracture with significant density contrasts. J. Contam. Hydrol. 120-121, 184–197. https://doi.org/10.1016/j.jconhyd.2010.08.002.

Bromly, M., Hinz, C., 2004. Non-Fickian transport in homogeneous unsaturated repacked sand. Water Resour. Res. 40 (7), 263. https://doi.org/10.1029/2003WR002579.

Chen, Y., Zhao, Z., 2020. Heat transfer in a 3D rough rock fracture with heterogeneous apertures. Int. J. Rock Mech. Min. Sci. 134, 104445.

Chen, Z., Qian, J., Zhan, H., Zhou, Z., Wang, J., Tan, Y., 2017. Effect of roughness on water flow through a synthetic single rough fracture. Environ. Earth Sci. 76 (4), 55. https://doi.org/10.1007/s12665-017-6470-7.

Chen, Y., Zhao, Z., Peng, H., 2022. Convective heat transfer of water flow in intersected rock fractures for enhanced geothermal extraction. J Rock Mech Geotech Eng 14 (1), 108–122.

Cherubini, C., Pastore, N., Giasi, C.I., Allegretti, N.M., 2017. Laboratory experimental investigation of heat transport in fractured media. Nonlin. Processes Geophys. 24 (1), 23–42. https://doi.org/10.5194/npg-24-23-2017.

Cirpka, O.A., Kitanidis, P.K., 2000a. Characterization of mixing and dilution in heterogeneous aquifers by means of local temporal moments. Water Resour. Res. 36 (5), 1221–1236. https://doi.org/10.1029/1999WR900354.

Cirpka, O.A., Kitanidis, P.K., 2000b. An advective-dispersive stream tube approach for the transfer of conservative-tracer data to reactive transport. Water Resour. Res. 36 (5), 1209–1220. https://doi.org/10.1029/1999WR900355.

Anon. COMSOL Userś guide (2012), Comsol multiphysic userś guide: version 4.3.

Constantz, J., Cox, M.H., Su, G.W., 2003. Comparison of heat and bromide as ground water tracers near streams. Ground Water 41 (5), 647–656.

De Marsily, G., 2004. Cours dhydrogéologie, 236 pp., Course notes. Reviewed and Improved from "Quantitative hydrogeology, Groundwater hydrology For Engineers. Academic Press, New York (1986).

Detwiler, R.L., Glass, R.J., Bourcier, W.L., 2003. Experimental observations of fracture dissolution: the role of Peclet number on evolving aperture variability. Geophys. Res. Lett. 30 (12), 283. https://doi.org/10.1029/2003GL017396.

Detwiler, R.L., Rajaram, H., Glass, R.J., 2000. Solute transport in variable-aperture fractures: an investigation of the relative importance of Taylor dispersion and macrodispersion. Water Resour. Res. 36 (7), 1611–1625. https://doi.org/10.1029/2000WR900036.

Fomin, S.A., Chugunov, V.A., Hashida, T., 2011. Non-Fickian mass transport in fractured porous media. Adv. Water Resour. 34 (2), 205–214. https://doi.org/10.1016/j.advwatres.2010.11.002.

Fourar, M., Radilla, G., 2009. Non-fickian description of tracer transport through heterogeneous porous media. Transp. Porous Med. 80 (3), 561–579. https://doi.org/10.1007/s11242-009-9380-7.

Frank, S., Heinze, T., Pollak, S., Wohnlich, S., 2021. Transient heat transfer processes in a single rock fracture at high flow rates. , Geothermics 89, 101989.

Gautam, P.-S., Mohanty, K.-K., 2004. Matrix–Fracture Transfer through Countercurrent Imbibition in Presence of Fracture Fluid Flow. Transp. Porous Media 55 (3), 309–337. https://doi.org/10.1023/B:TIPM.0000013326.95597.10.

Ge, S., 1997. A governing equation for fluid flow in rough fractures. Water Resour. Res. 33 (1), 53–61. https://doi.org/10.1029/96WR02588.

Geiger, S., Emmanuel, S., 2010. Non-Fourier thermal transport in fractured geological media. Water Resour. Res. 46 (7), 143. https://doi.org/10.1029/2009WR008671.

Gelhar, W., Welty, C., Rehfeldt, K.R., 1992. A critical review of data on field-scale dispersion in aquifers. Water Resour. Res. 28 (7), 1955–1974. https://doi.org/10.1029/92WR00607.

González-Pinzón, R., Haggerty, R., Dentz, M., 2013. Scaling and predicting solute transport processes in streams. Water Resour. Res. 49 (7), 4071–4088. https://doi.org/10.1002/wrcr.20280.

Gossler, A.M., Peter Bayer, B., Zosseder, K, 2019. Experimental investigation of thermal retardation and local thermal nonequilibrium effects on heat transport in highly permeable, porous aquifers. J. Hydrol. 578, 124097 https://doi.org/10.1016/j.jhydrol.2019.124097.

Gouze, P., Le Borgne, T., Leprovost, R., Lods, G., Poidras, T., Pezard, P., 2008. Non-Fickian dispersion in porous media: 1. Multiscale measurements using single-well injection withdrawal tracer tests. Water Resour. Res. 44 (6), 3293. https://doi.org/10.1029/2007WR006278.

Guihéneuf, N., Bour, O., Boisson, A., Le Borgne, T., Becker, M.W., Nigon, B., Wajiduddin, M., Ahmed, S., Maréchal, J.-C., 2017. Insights about transport mechanisms and fracture flow channeling from multi-scale observations of tracer dispersion in shallow fractured crystalline rock. J. Contam. Hydrol. 206, 18–33. https://doi.org/10.1016/j.jconhyd.2017.09.003.

Heinze, T., Hamidi, S., Galvan, B., 2017. A dynamic heat transfer coefficient between fractured rock and flowing fluid. Geothermics 65, 10–16.

Klepikova, M.V., Le Borgne, T., Bour, O., Dentz, M., Hochreutener, R., Lavenant, N., 2016. Heat as a tracer for understanding transport processes in fractured media: theory and field assessment from multiscale thermal push-pull tracer tests. Water Resour. Res. 52 (7), 5442–5457. https://doi.org/10.1002/2016WR018789.

Klepikova, M.V., Méheust, Y., Roques, C., Linde, N., 2021. Heat transport by flow through rough rock fractures: a numerical investigation. Adv. Water Resour. 156, 104042 https://doi.org/10.1016/j.advwatres.2021.104042.

Jaoude, I.B., Novakowski, K., Kueper, B., 2022. Comparing heat and solute transport in a discrete rock fracture of variable aperture. J. Hydrol. 607, 127496.

Liu, R., He, M., Huang, N., Jiang, Y., Yu, L, 2020. Three-dimensional double-rough-walled modeling of fluid flow through self-affine shear fractures. J. Rock Mech. Geotech. Eng. 12 (1), 41–49.

Luo, S., Zhao, Z., Peng, H., Pu, H., 2016. The role of fracture surface roughness in macroscopic fluid flow and heat transfer in fractured rocks. Int. J. Rock Mech. Min. Sci. 87, 29–38.

Luo, J., Qi, Y., Zhao, Q., Tan, L., Xiang, W., Rohn, J., 2018. Investigation of flow and heat transfer characteristics in fractured granite. Energies 11, 1228.

Luo, Y., Xu, W., Lei, Y., Wu, P., Qin, Q., Ba, R., 2019. Experimental study of heat transfer by water flowing through smooth and rough rock fractures. Energy Reports 5, 1025–1029.

Ma, R., Zheng, C., Zachara, J.M., Tonkin, M., 2012. Utility of bromide and heat tracers for aquifer characterization affected by highly transient flow conditions. Water Resour. Res. 48 (8), 951. https://doi.org/10.1029/2011WR011281.

Molina-Giraldo, N. (2001), Heat transport modeling in shallow aquifers: the role of thermal dispersion in aquifers and heat conduction into confining layers.

Mourzenko, V.V., Thovert, J.-F., Adler, P.M., 1995. Permeability of a single fracture; validity of the reynolds equation. J. Phys. II France 5 (3), 465–482. https://doi.org/10.1051/jp2:1995133.

Neretnieks, I., 1980. Diffusion in the rock matrix: an important factor in radionuclide retardation? J. Geophys. Res. 85 (B8), 4379–4397. https://doi.org/10.1029/JB085iB08p04379.

Neuville, A., Toussaint, R., Schmittbuhl, J., 2010. Fracture roughness and thermal exchange: a case study at Soultz-sous-Forêts. C.R. Geosci. 342 (7–8), 616–625. https://doi.org/10.1016/j.crte.2009.03.006.

Neuville, A., Toussaint, R., Schmittbuhl, J., 2011. Hydraulic transmissivity and heat exchange efficiency of rough fractures: a model based on low pass filtered apertures. Geophys. J. Int.

Nigon, B., Englert, A., Pascal, C., Saintot, A., 2017. Multi-scale characterization of joint surface roughness. J. Geophys. Res. Solid Earth. https://doi.org/10.1002/2017JB014322.

Nigon, B., Englert, A., Pascal, C., 2019. Three-dimensional flow characterization in a joint with plumose pattern. Hydrogeol. J. 27, 87–99.

Okoroafor, E.R., Co, C., Horne, R.N., 2022. Numerical investigation of the impact of fracture aperture anisotropy on EGS thermal performance. Geothermics 100, 102354. https://doi.org/10.1016/j.geothermics.2022.102354.

Pascal, C., 2021. Paleostress Inversion Techniques: Methods and Applications for Tectonics. Elsevier, p. 274.

Pascal, C., Angelier, J., Cacas, M.-C., Hancock, P.L., 1997. Distribution of joints: probabilistic modelling and case study near Cardiff (Wales, U.K.). J. Struct. Geol. 19 (10), 1273–1284. https://doi.org/10.1016/S0191-8141(97)00047-3.

Rau, G.C., Andersen, M.S., Acworth, R.I., 2012. Experimental investigation of the thermal dispersivity term and its significance in the heat transport equation for flow in sediments. Water Resour. Res. 48 (3), 951. https://doi.org/10.1029/2011WR011038.

Read, T., Bour, O., Bense, V., Le Borgne, T., Goderniaux, P., Klepikova, M.V., Hochreutener, R., Lavenant, N., Boschero, V., 2013. Characterizing groundwater flow and heat transport in fractured rock using fiber-optic distributed temperature sensing. Geophys. Res. Lett. 40 (10), 2055–2059. https://doi.org/10.1002/grl.50397.

Renshaw, C.E., 1995. On the relationship between mechanical and hydraulic apertures in rough-walled fractures. J. Geophys. Res.

Roux, S., Plouraboué, F., Hulin, J.-P., 1998. Tracer dispersion in rough open crack. Transp. Porous Media 32 (1), 97–116.

Taylor, G., 1953. Dispersion of soluble matter in solvent flowing slowly through a tube. Proc. R. Soc. A: Math. Phys. Eng. Sci. 219 (1137), 186–203. https://doi.org/10.1098/rspa.1953.0139.

Vandenbohede, A., Louwyck, A., Lebbe, L., 2009. Conservative solute versus heat transport in porous media during push-pull tests. Transp. Porous Med. 76 (2), 265–287. https://doi.org/10.1007/s11242-008-9246-4.

Wang, J.S.Y., Narasimhan, T.N., 1985. Hydrologic mechanisms governing fluid flow in a partially saturated, fractured, porous medium. Water Resour. Res. 21 (12), 1861–1874. https://doi.org/10.1029/WR021i012p01861.

Woodbury, A.D., Smith, L., 1985. On the thermal effects of three-dimensional groundwater flow. J. Geophys. Res. 90 (B1), 759–767. https://doi.org/10.1029/JB090iB01p00759.

Zhou, Q., Liu, H.-H., Molz, F.J., Zhang, Y., Bodvarsson, G.S., 2007. Field-scale effective matrix diffusion coefficient for fractured rock: results from literature survey. J. Contam. Hydrol. 93 (1–4), 161–187. https://doi.org/10.1016/j.jconhyd.2007.02.002.

Zou, L., Jing, L., Cvetkovic, V., 2017. Modeling of solute transport in a 3D rough-walled fracture–matrix system. Transp. Porous Med. 116 (3), 1005–1029. https://doi.org/10.1007/s11242-016-0810-z.